Schleicher, A. M., Jurado, M. (2019): Linking faults, fractures and clay mineral occurrence with fluid transport in the accretionary prism of the Nankai Trough, Japan. - *Geochemistry Geophysics Geosystems (G3)*, *20*, 11, pp. 4599—4612.

DOI: http://doi.org/10.1029/2019GC008430

Geochemistry, Geophysics, Geosystems

RESEARCH ARTICLE
10.1029/2019GC008430

Linking Faults, Fractures, and Clay Mineral Occurrence With Fluid Transport in the Accretionary Prism of the Nankai Trough, Japan

Anja M. Schleicher[1] **and Maria-Jose Jurado**[2]

[1]Helmholtz Zentrum Potsdam, Deutsches GeoForschungsZentrum (GFZ), Potsdam, Germany, [2]Instituto de Ciencias de la Tierra Jaume Almera CSIC, Barcelona, Spain

Key Points:
- Faults and fractures in the accretionary prism of the Nankai Trough are localized pathways for fluids
- The formation of clay minerals occurs within the range of the faulted and fractured zones
- The linkage of local deformation and clay formation has implications for fluid-rock interaction in fractured areas of an accretionary prism

Correspondence to:
A. M. Schleicher,
anja.schleicher@gfz-potsdam.de

Citation:
Schleicher, A. M., & Jurado, M.-J. (2019). Linking faults, fractures, and clay mineral occurrence with fluid transport in the accretionary prism of the Nankai Trough, Japan. *Geochemistry, Geophysics, Geosystems*, *20*, 4599–4612. https://doi.org/10.1029/2019GC008430

Received 3 MAY 2019
Accepted 19 AUG 2019
Accepted article online 14 OCT 2019
Published online 5 NOV 2019

Abstract The interpretation of logging while drilling resistivity oriented images and geophysical logs from Hole C0002 drilled during the International Ocean Discovery Program (IODP) Expeditions 338 and 348 of the Nankai Trough Seismogenic Zone Experiment (NanTroSEIZE) project revealed a complex structure of the accretionary prism characterized by steep bedding and abundant folds and fault zones, indicative of specific areas of deformation within the clay-dominated prism sediments. Local faults were undoubtedly interpreted on images from Hole C0002P (2,162.5–3,058.4 m below seafloor), whereas folds were identified in both Holes C0002P and C0002F (860–2,005.5 m below seafloor). The clay mineral analysis of rock samples (cuttings) shows that clay mineralization occurs within the range of the faulted and fractured zones. This linkage between local deformation and clay mineralization can have implications for enhanced fluid flow and localized fluid-rock interaction within the highly fractured areas of the accretionary prism. We conclude that dissolution and neomineralization of illitic and smectitic phases within fractures and faults is a process that probably continues during active creep and fault reactivation and plays a key role in influencing weak fault and creep behavior within the Nankai Trough, and likely in shallow fault systems elsewhere.

1. Introduction

Oceanic accretionary prisms in the Earth's crust generally consist of marine sediments with areas of undisturbed consolidated rock material, and areas of intense internal rock deformation down to the main plate boundary fault (Boston et al., 2016; Davis et al., 1983; Kimura et al., 2007). The fluids that circulate within such prisms derive largely from sediment consolidation and mineral dehydration, as well as methane and carbon dioxide generations from organic matter (Bird, 1984; Kitajima & Saffer, 2014; Raimbourg et al., 2015). While they generally tend to follow the paths of least resistance in their passage through low permeability formations, they can significantly affect porosity, heat transport, transport of solutes, and mineral alteration within the sediments (Kastner et al., 1991; Saffer & Bekins, 1998).

When these sediments are transected by a number of permeable faults or interconnected fractures, the fluids tend to follow pathways along those fault rocks, causing enhanced alteration due to transformation—and/or dissolution-precipitation reactions within the rock, and thus largely influence the hydro-mechanical behavior of the fault system (e.g., Evans & Chester, 1995; Faulkner et al., 2010; Vrolijk & van der Pluijm, 1999). In fact, the formation of a variety of clay minerals is often coupled with a strong fluid conduit or fluid barrier behavior in the fault, or a displacement of faults within the major fault structures (Caine et al., 1996; Moore & Vrolijk, 1992; Wu et al., 1975). Whereas the majority of the clay minerals in accretionary prisms are generally detrital illite, chlorite, smectite, and mixed-layered varieties (Underwood, 2007; Underwood & Pickering, 1996), such clays can also precipitate from fluids or transform from primary minerals such as feldspar or mica. A global compilation of clay mineralogical data in subduction zones also suggests that particularly smectite-rich clay minerals are major players for fluid-rock interaction processes in the temperature interval between 50 and 150 °C within the prism (Vrolijk, 1990).

During the International Ocean Discovery Program (IODP) Expeditions 338 and 348, where drilling occurred at Site C0002 down to 3,058.5 m below seafloor (mbsf), sampling of clay-rich rocks from the inner accretionary prism of the Nankai Trough took place (Strasser et al., 2013; Tobin et al., 2015). The prism, which is located south-east of Japan's island Honshu (Figure 1a), is characterized by an outer wedge comprising strongly deformed sediments with an aseismic décollement, and an inner wedge with rather

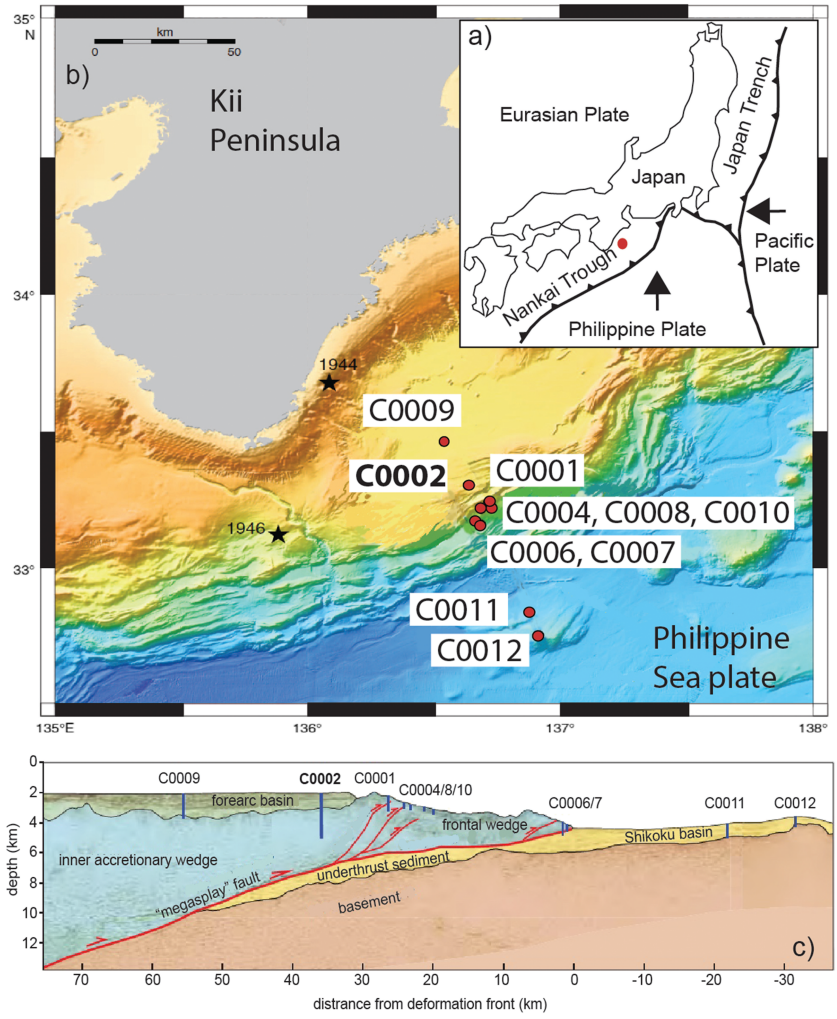

Figure 1. (a) Map of Japan with the Nankai Trough subduction zone offshore Kii peninsula. The red dot shows the location of the Nankai Trough Seismogenic Zone Experiment (NanTroSEIZE) experiment; (b) International Ocean Discovery Program (IODP) drill sites and locations; the black stars show epicenters in the Nankai Trough in the years 1944 and 1946 (modified after Ryan et al., (2009)); (c) cross section through the Nankai Trough, showing Site C0002 in relation to other NanTroSEIZE Sites (modified from Exp. 348 Scientists, 2014).

weakly deformed sediments underneath the Kumano forearc basin (Boston et al., 2016). A well-developed megasplay fault bounds the inner and the outer prism (Park et al., 2002; Strasser et al., 2009). In this study, we link the abundance of fractures and faults with the occurrence of newly formed clay minerals in the deep section of the Nankai Trough inner accretionary prism. In fact, mineral precipitation can occur in such faults and fractures and are often mixed with detrital clay minerals off-scraped from adjacent subducting sediments (Hüpers et al., 2019). However, although clay minerals are to be known as very important components in faults and fractures of an accretionary prism, the link between clay occurrence, faulting processes, and fluid pathways is still under debate (e.g., Raimbourg et al., 2015; Saffer et al., 2008; Toki et al., 2014).

1.1. The Nankai Trough Subduction Zone and the NanTroSEIZE Project

In the Nankai Trough subduction zone, the Philippine Sea Plate subducts underneath the Eurasian Plate (Seno et al., 1993), with a plate boundary megathrust fault as a possible source of devastating earthquakes (Figure 1). The latest large earthquakes in the Nankai Trough with Tonankai in the year 1944 and Nankaido in 1946 involved coseismic slip on a splay fault with a magnitude of M>8 (Kanamori, 1972; Baba et al., 2006; Figure 1b). These displacements typically cause changes in pressure, temperature, fluid

activity and internal deformation in the accretionary prism (Boston et al., 2016). The IODP Nankai Trough Seismogenic Zone Experiment (NanTroSEIZE) drilling project, which aims to improve our understanding on the mechanics of stress accumulation and rupture propagation along the Nankai accretionary prism, samples, and instruments the seismogenic portion of the accretionary prism (Kinoshita et al., 2009; Tobin & Kinoshita, 2006). Several holes have been drilled on the upper plate and the subducting plate of the subduction zone (Figures 1b and 1c). Site C0002, which is located along the seaward side of the Kumano basin and drilled via both non-riser drilling and riser drilling in multiple stages during Expeditions 314, 315, 326, 338, and 348, contains a number of holes of different depths (e.g., Kinoshita et al., 2009; Moore et al., 2014; Strasser et al., 2013; Tobin et al., 2015).

The Holes C0002F, C0002N, and C0002P were drilled during Expeditions 338 and 348 in NanTroSEIZE Stage 3 (Strasser et al., 2013; Tobin et al., 2015). Expedition 338 extended drill hole C0002F from 860 to 2,005.5 mbsf using a drill bit and an underreamer. The offset between the drill bit and the cutting portion of the underreamer was 43.8 m, causing an unavoidable mixing of cuttings. The hole was abandoned due to the damage of the riser system before the installation of the casing. A full suite of logging-while-drilling (LWD) and measurement-while-drilling (MWD) tools collected gamma ray and resistivity logs, *P*-wave velocity data, azimuthal resistivity data and borehole resistivity images. Mud gas was analyzed during drilling, and the mineralogy and geochemistry of cutting samples was characterized every 10 m (Strasser et al., 2013). During Expedition 348, Hole C0002N was side-tracked from the casing of Hole C0002F and drilled from 856 to 2,325.5 mbsf with a drill bit only. LWD (only resistivity and gamma ray), MWD, mud-gas and cuttings were collected. Due to the difficulty of deepening the hole below the casing shoe, Hole C0002N was abandoned, and Hole C0002P was side-tracked from Hole C0002N at 2,162.5 mbsf and deepened to 3,058.4 mbsf with a drill bit only and a full suite of LWD. The interval from 2,163 to 2,218 mbsf was cored at Hole C0002P with the rotary core barrel (RCB) (Tobin et al., 2015).

In this study, we explore the connection between the clay mineralization and the association with fluid flow in fractured and faulted zones. Our analysis is based on the post-cruise evaluation and interpretation of the LWD borehole data set and specific clay-mineralogical analyses of cuttings samples. It uses the datasets acquired at Site C0002F and C0002P during Expeditions 338 and 348, including LWD oriented images, geophysical logs and clay mineralogical data (Strasser et al., 2013; Tobin et al., 2015). Because of limited LWD datasets, logging data and cutting samples from Hole C0002N were not used.

2. Sampling Strategy and Analytical Methods

At Hole C0002F, 41 washed cuttings samples from different depths were taken between 935.5 mbsf drill bit depth and 2,000.5 m bsf drill bit depth (Table 1). The use of an underreamer compromised the possibility to establish a precise depth match between the cuttings depths and the logging data. For this reason, more reliable and better depth-constrained cuttings analyses resulted from Hole C0002P, where reaming-while-drilling was not implemented. A total of 47 washed cuttings samples were taken from Hole C0002P between 2,065.5 mbsf and 3,015.5 mbsf (cuttings #36-291; Table 1). All samples were chosen based on the macroscopic and microscopic observations of the clay content and the mineralogical and geochemical analyses of the bulk minerals and the element distribution aboard, as well as shipboard logging data acquired during the expeditions. Exclusively silty claystone samples were sampled for comparison, as they contain abundant clay minerals.

Semiquantitative bulk X-ray diffractometer (XRD) measurements on cuttings were conducted aboard during both Expeditions 338 and 348, with analyses of total clay minerals, quartz, feldspar and calcite. The cuttings were rinsed with seawater and washed with deionized water on board, in order to avoid drill mud contamination. The analysis was examined on powdered cuttings from the 1–4 mm size fraction. For a more detailed explanation of the sample preparation and results description on board see Strasser et al. (2013) and Tobin et al. (2015). After the expedition, the cuttings were thoroughly washed again with deionized water, and the drilling induced clay aggregates were removed at the University of Michigan. The clay size fraction (<2 μm) was separated using a standard centrifuge. All XRD analyses of the random powder and texture (oriented) preparation followed the analytical methods described in Moore and Reynolds (1997). Oriented clay size samples were measured under air-dried and glycolated conditions, the latter treatment caused interlayer expansion of swelling clays, allowing the recognition of smectite and mixed-layer smectitic phases. In

Table 1
Clay Mineral Data Based on XRD Intensity Measurements

Depth (mbsf) C0002F	Sample (SMW)	Smectite (int./cps)	Illite (int./cps)	Depth mbsf C0002P	Sample (SMW)	Smectite (int./cps)	Illite (int./cps)
1,195.5	82	386	399	2,345.5	133	189	345
1,235.5	92	320	284	2,355.5	136	247	350
1,285.5	102	258	323	2,365.5	138	83	242
1,335.5	112	171	282	2,375.5	141	658	744
1,345.5	114	254	257	2,385.5	143	529	985
1,365.5	120	259	203	1,295.5	145	504	736
1,375.5	122	259	328	2,405.5	149	238	689
1,385.5	124	289	285	2,415.5	151	148	313
1,395.5	126	253	287	2,425.5	155	426	730
1,435.5	136	255	310	2,465.5	163	107	223
1,485.5	148	295	254	2,515.5	174	128	321
1,515.5	155	267	366	2,565.5	185	178	354
1,535.5	161	321	337	2,595.5	191	233	726
1,545.5	163	260	388	2,605.5	196	254	461
1,585.5	174	192	312	2,615.5	198	167	559
1,635.5	189	181	281	2,625.5	200	971	1248
1,685.5	203	247	216	2,635.5	202	516	885
1,705.5	207	194	309	2,645.5	204	478	978
1,735.5	213	248	272	2,655.5	208	435	883
1,785.5	227	264	297	2,665.5	210	194	356
1,835.5	238	369	294	2,675.5	213	657	1216
1,875.5	255	287	407	2,685.5	215	748	1177
1,885.5	258	359	343	2,695.5	217	983	1512
1,925.5	267	350	426	2,705.5	219	633	1540
1,935.5	269	397	284	2,715.5	221	119	336
1,945.5	272	322	265	2,725.5	224	540	1305
1,985.5	284	373	398	2,735.5	226	550	1266
2,000.5	288	305	407	2,745.5	229	992	1925
				2,755.5	231	867	1633
Depth (mbsf) C0002P	Sample (SMW)	Smectite (intensity)	Illite (intensity)	2,765.5	233	110	431
				2,775.5	235	543	1262
2,065.5	36	128	307	2,785.5	237	542	1371
2,115.5	53	313	697	2,795.5	240	519	1456
2,165.5	71	561	773	2,805.5	242	303	1217
2,215.5	86	134	346	2,815.5	244	201	745
2,265.5	115	139	264	2,865.5	256	182	521
2,315.5	127	129	237	2,915.5	267	158	493
2,325.5	129	1532	1288	2,965.5	279	100	482
2,335.5	131	803	656	3,015.5	291	230	583

Note. The depth is displayed in meter below surface (mbsf); the sample number SMW (solid cuttings taken from drilling mud) is the sample identification; the intensity of illite and smectite is displayed in cps (counts per second).
Abbreviation: XRD: X-ray diffractometer.

order to compare the clay mineral content, and the mineral amount relative to the adjacent material, exactly 45 μg of material was mixed with 1.5-ml deionized water and dropped on a round glass slide (diameter 32 mm). All air-dried samples were measured at a relative humidity of ~30 %, and afterward stored in a desiccator filled with ethylene glycol, in order to investigate the final swelling stage of the smectitic phases. Intensity (counts per second, Table 1), *d*-value changes (nm), and if possible half width broadening (FWHM) of the particular clay peak was determined. The XRD raw files are stored in "GFZ Data Services" (Schleicher & Jurado, 2019).

The clay minerals were identified and analyzed using a Rigaku Ultima IV XRD housed at the University of Michigan for samples from Holes C0002F and C0002P, and a PANalytical Empyrean XRD at the GeoForschungsZentrum (GFZ) Potsdam, Germany for samples from Hole C0002P. Both machines are operating at 40 kV and 40–44 mA with Cu-Kα radiation. The samples were analyzed with the Bragg-Brentano geometry between 2° and 50 °2θ (air dried) or 2° and 20 °2θ (ethylene glycol) and a step-width of 0.01/0.02 °2θ. The samples (mineralogy, *d*-value, FWHM values, and intensity) were analyzed using the program "EVA" (Bruker).

Scanning electron microscopy (SEM) analyses were conducted on selected carbon-coated cutting samples on board the Chikyu during Expedition 348. The SEM is a JEOL JCM-5700LV machine with a resolution of 5.0 nm and a magnification of up to 30,000x. It is equipped with a EDS (energy-dispersive spectroscopy) for chemical analyses. Transmission electron microscopy (TEM) analyses were conducted with a FEI Tecnai G2 F20 X-Twin transmission electron microscope (TEM/AEM), equipped with a Gatan Tridiem energy filter, a Fischione high-angle annular dark field detector (HAADF), and an energy-dispersive X-ray analyzer (EDS) at the GFZ Potsdam. After impregnation of the sample with carbon, it was cut using a focused ion beam (FIB) device (FEI FIB200TEM; for more detailed information, see Wirth (2009)).

The logging data were acquired during Expedition 338 at Hole C0002F down to 2,005.5 mbsf, using logging while drilling (LWD) tools (Strasser et al., 2013). Natural gamma ray, electrical resistivity, sonic velocity and resistivity oriented images were used for detailed examination and interpretation. Expedition 348 used similar LWD tools (Tobin et al., 2015). Additionally, the azimuthal focused resistivity (AFR) borehole-imaging tool produced a high-resolution resistivity image acquired in 128 discrete azimuthal bins with an ideal 10 mm image resolution (Tobin et al., 2015). The LWD resistivity oriented images from Holes C0002F and C0002P have been processed and analyzed post-cruise to define major lithological changes and stratigraphic boundaries, and to characterize the internal accretionary prism structures intersected at Site C0002 by defining the geometry and the orientation of bedding planes, fractures and faults. Also a detailed analysis for detection of possible open, fluid conductive structures was conducted. The interpretation of the resistivity oriented images allowed us to outline the structure intersected at Site C0002 (shown in figures 5 and 6).

3. Results

3.1. Mineralogy

The XRD bulk rock analyses carried out on cuttings aboard Chikyu during Expeditions 338 and 348 revealed an overall mineralogy with quartz, feldspar and clay minerals (Strasser et al., 2013; Tobin et al., 2015). The total clay content of around 65 % in average was analyzed, with specific areas of higher clay contents up to ~70 wt% at ~1,000 mbsf and ~1,350 mbsf, as well as at ~1,950 mbsf, at ~2,300 mbsf, and at ~2,700 mbsf (Figure 2a). The mineralogy of the <2-μm clay-size fraction analyzed at the University of Michigan and the GFZ Potsdam consists of a very smectite-rich illite-smectite, illite, chlorite, and kaolinite (Figure 2b). The clay minerals illite and smectite-rich illite-smectite are the main constituents in both boreholes with relative changes in intensity (counts per seconds, cps; Table 1) in the x-ray patterns at certain depths, reflecting an increase or decrease of clay in relation to the adjacent samples (Figures 2c and 6c and Table 1). Based on these changes in the relative peak intensities, a relative increase is observed at ~1,300–1,400 mbsf, 1,750 mbsf, 2,250–2.300 mbsf, and 2,500–2,700 mbsf (Figure 2b). These depths are in relative agreement with an increase of total clay observed during Expeditions 338 and 348 (Strasser et al., 2013; Tobin et al., 2015).

Figure 2c shows selected XRD patterns of the clay size fraction (<2 μm) of specific cuttings from 1,345.5 mbsf (SMW 114) and 1,945 mbsf (SMW 272, Hole C0002F), as well as from 2325.5 m (SMW 129) and 2695.5 m (SMW 217, Hole C0002P). Whereas the illite clay minerals show a characteristic peak at 1.0 nm (8.8 °2θ) both in the air dried state and after ethylene glycolation, a shared characteristic peak of 002 chlorite and 001 kaolinite occurs at 0.71 nm (12.3 °2θ). The smectite-rich illite-smectite clay minerals shows characteristic 00l peaks between 1.26 and 1.29 nm (7.0–6.8 °2θ) in the air dried state, reflecting 2 water layers in the smectite interlayers. These peaks shift to 1.68–1.72 nm (5.25–6.0 °2θ) after ethylene glycolation, with 2–3 water layers. Because of the occurrence of a weak characteristic peak at 0.88 nm (10 °2θ), it is not pure smectite, but a smectite-rich illite-smectite (see also Hüpers et al. (2019)).

3.2. Microstructures in Cutting Samples

Distinct microstructures of the selected rock cuttings of silty claystone collected from a fractured area at ~2,700 mbsf in Hole C0002P were observed (Figure 3). Thin fractures that occur mostly parallel or in low angles to the bedding plane are visible by eye and up to several mm thick (Figure 3a). These fractures are not drilling induced fractures, as they show distinct polished surfaces also inside the closed fractures. Also, secondary electron microscopy (SEM) imaging reveals a variety of much finer fractures and faults in a matrix of illite and smectite-rich illite/smectite clay minerals. Most fractures and faults crosscut in low angles or parallel to the bedding plane (Figures 3b and 3c). In many rock chips, slickenlines occur on shiny polished fracture surfaces (Figure 3d), representing mechanical striations that can develop during faulting.

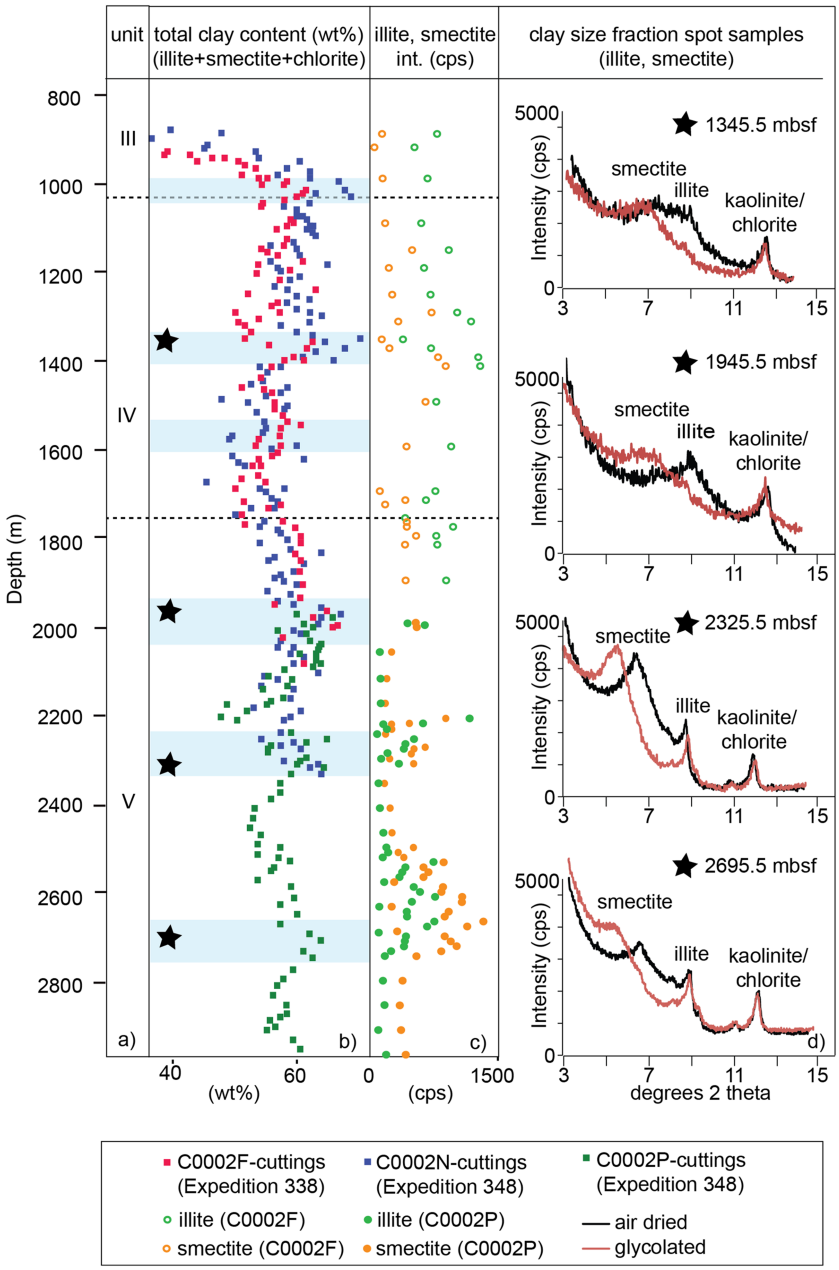

Figure 2. X-ray diffractometer data of International Ocean Discovery Program (IODP) Site C0002 from 800 to 3,058 mbsf showing (a) the three lithological units defined during Expeditions 338 and 348; (b) total clay mineral content in Holes C0002F (Expedition 338; Strasser et al., 2013), and Holes C0002N, and C0002P (Expedition 348; Tobin et al., 2015). The black stars represent the locations of four representative clay samples in 2d); (c) illite (green) and smectitic (orange) intensities based on X-ray diffractometer measurements of the clay-size fraction; (d) representative clay mineral samples containing illite, smectite, and kaolinite in air-dried state (black) and after glycolization (red).

The surface structure shows differences in step length, step height, shininess and orientation to bedding. Along and adjacent to the fractures occur illite and smectite with different particle shapes, sizes and microstructural features. Relatively large detrital illite/mica minerals occur as well in the matrix (Figure 3c), whereas pseudohexagonal illite and/or illite-smectite with irregular sutured crystal edges occur in pores (Figure 3e). Smectite particles are shown as thin wavy layers without a visible structure or shape (Figure 3f). The TEM analyses confirm the deformation features and heavy fracturation determined in the SEM. Discrete illite and smectite crystals were observed; illite is often bended and kinked

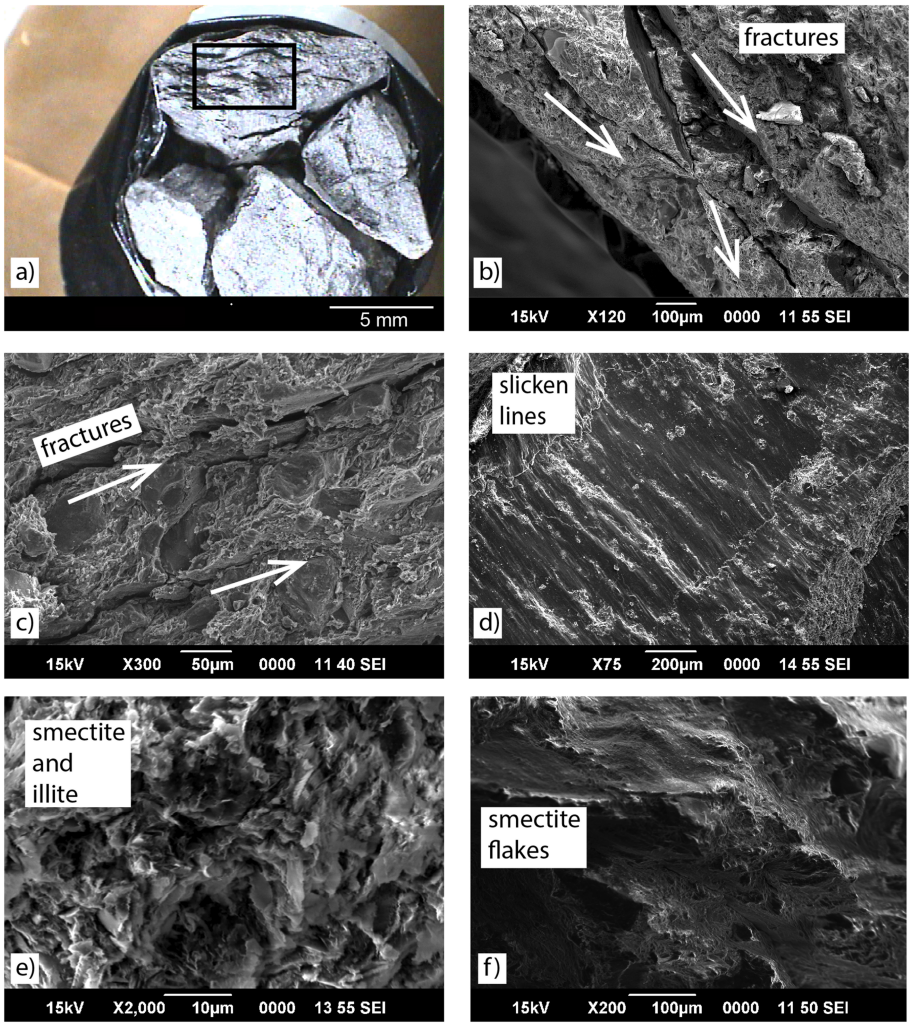

Figure 3. Scanning electron microscopy pictures of mudrock cuttings taken from 2,580 to 2,830 mbsf at Hole C0002P: (a) low angle to parallel fractures are visible by eye and up to several mm thick; (b) secondary electron (SE) image of fine fractures in a matrix of illite and smectite; (c) fine fractures oriented parallel to the bedding plane; (d) slickenlines on shiny polished fracture surfaces; (e) smectite and illite flakes as pore fillings with irregular sutured crystal edges; (f) smectite particles are shown as thin wavy layers without a visible structure or shape.

(Figures 4a and 4b), whereas smectite shows mostly wavy structures with often friable and frayed features (Figure 4d).

3.3. Comparing Fracture and Fault Distribution Characterized by Logging With Clay Mineralogy

Whereas the detailed characterization of selected cuttings gives information about the mineralogy and the microstructures at specific depths, the logging data provide continuous and depth-constrained information on the compositional and textural features, and also on geometries and the structures of the rocks in the accretionary prism. Figures 5 and 6 display the image and log interpretation results together with XRD intensity data of illite and smectite-rich illite-smectite from Holes C0002F and C0002P, allowing the comparison and correlation with the clay mineralogy investigated at local depths.

LWD resistivity oriented images show that bedding orientation is steeply dipping NW (> 60°) with several zones of disruption throughout Site C0002 (Figures 5a and 6a). In Hole C0002F, these disruptions and changes in dip attitude can be noticed at around 950, 1,350, 1,600, and 1,900 mbsf (Figure 5a and stars). In Hole C0002P, two distinct zones with changing dip can be observed at ~2,250 and ~2,700–2,750 mbsf. Here, the dip magnitudes are clearly disrupted and bedding orientation changes down to ~2,810 mbsf (Figure 6a). These zones correspond to the deformed zones characterized also by high fracture and fault

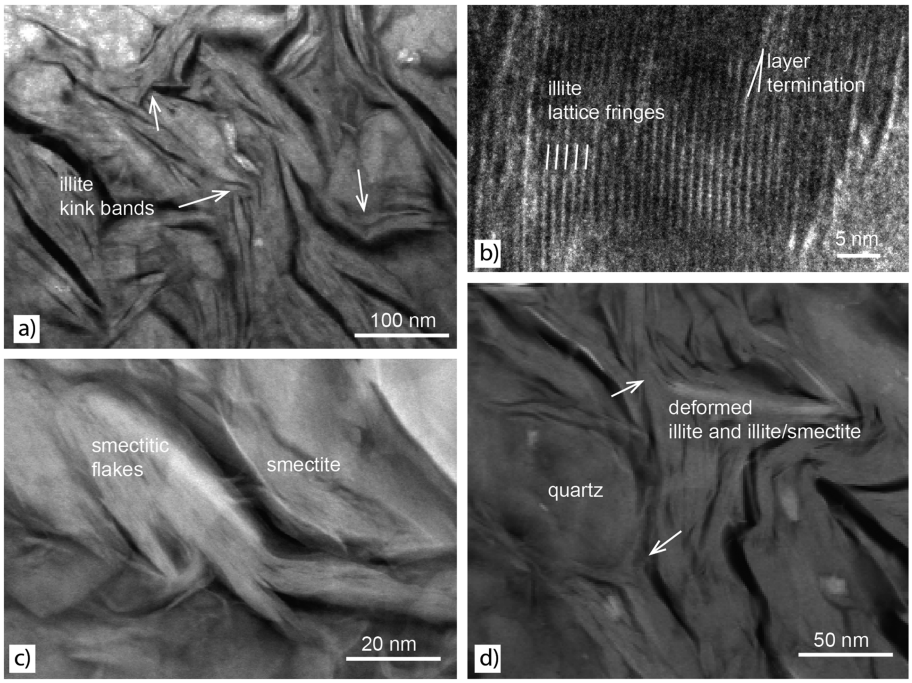

Figure 4. Transmission electron microscopy images of mudrock cuttings taken 2,580–2,830 mbsf at Hole C0002P: (a) fractured and deformed illite crystals, forming kink bands; (b) illite lattice fringes with the typical distance of 1 nm. Lattice defects as layer terminations are common; (c) friable and frayed smectitic clay; (d) deformed illite surrounding quartz particles.

density according to the structural interpretation of the LWD images (Figures 5d–5g and 6d–6g). Intense deformation can also be related to changes in resistivity shown by the darker areas that are higher conductive with a fairly uniform sediment composition, indicative of higher density of faults and fractures and/or a higher amount of fluids and clay minerals (Figures 5b and 6b). These dark bands can easily be correlated with intensely faulted and fractured zones, but are more difficult to correlate with the clay amount also due to different vertical sampling and resolution of the techniques and results. The correlation with the clay abundance is somehow more difficult to establish because of the different resolution and sampling when comparing logging data and cutting samples.

Within Hole C0002F, a low increase in illite/smectite and illite intensity could be observed in samples at 950, ~1,150, ~1,550, and ~1,900 mbsf, suggesting some authigenic clay formation (Figure 5c). However, the rather homogeneous intensities, as well as the slight difference to the bulk cuttings XRD analyses (Figure 2b) is most likely caused by the usage of the underreamer, which induced a distinct mix of cuttings (Strasser et al., 2013). A much better correlation to the bulk XRD analyses of total clay can be observed in Hole C0002P (Figure 6c), where the intensity of fractures and faults (Figures 6d and 6f) correlates with the intensity change in smectite and illite at around ~2,350–2,430 mbsf, and 2,580–2,810 mbsf, suggesting clay formation. A change of dip in the bedding planes at 2,300 mbsf and strong changes at 2,580 and 2,700 mbsf (Figure 6a) also indicate a high amount of fractures and faults in these areas. Finally, the bulk clay minerals show an increase in total clay content at 2250–2,350 mbsf and 2,650–2,750 mbsf (Figure 2b).

Conductive and resistive fractures irregularly extend throughout Hole C0002F (Figures 5d–5f), with increased conductive fracture count clusters at ~1,150, 1,350, and 1,610 mbsf, and a general trend to increasing amounts of fractures between 1,800 and 2,000 mbsf. Hole C0002P in Figures 6d and 6f, however, shows an increased amount of faults and fractures in more distinct areas. Increased fault intensities were detected at ~2,380–2,400 mbsf, 2,580–2,610 mbsf, and 2,700–2,900 mbsf, and fractures clusters were observed at ~2,310–2,370 mbsf, between 2,560 and 2,810 mbsf, and 2,900–2,950 mbsf. In fact, areas with higher quantities of faults are clearly located in the deformation zone between 2,580 and 2,810 mbsf, where bedding is more variable and clay minerals show increased intensities reflecting higher abundance. A higher amount

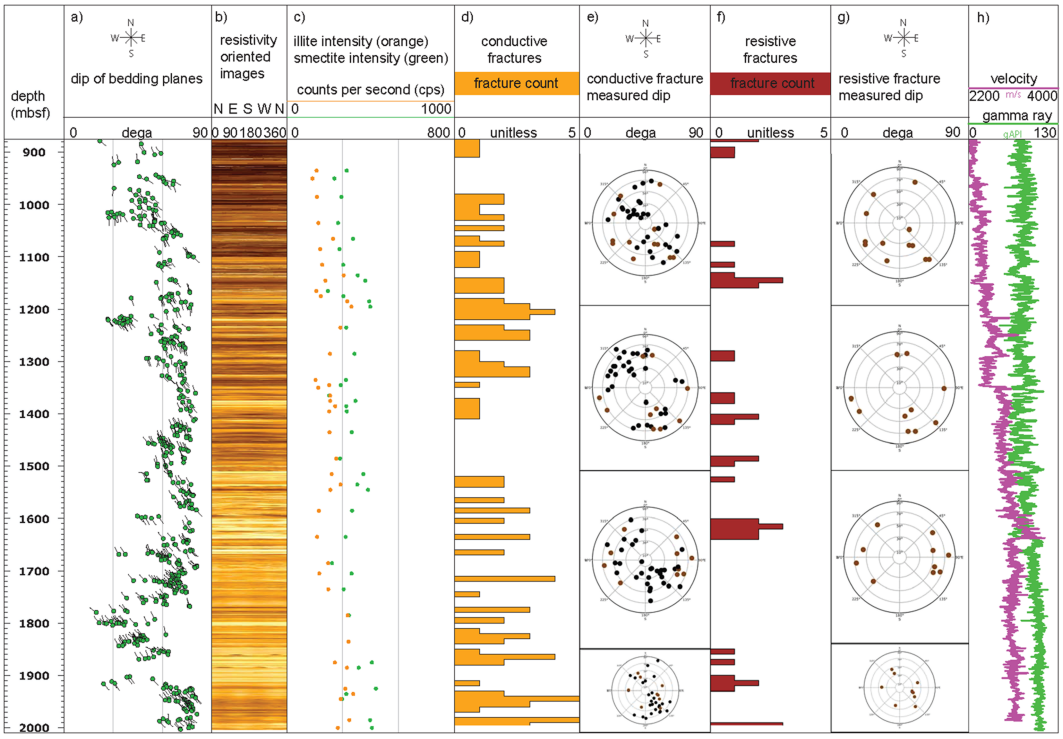

Figure 5. Logging data and mineralogical analyses of Hole C0002F between 880 and 2,010 mbsf. (a) bedding orientation tadpole plot of bedding planes measured on LWD image; (b) LWD resistivity oriented images; (c) illite and smectite intensity; (d) conductive fracture intensity indicated by the number of fracture planes within 10 m; (e) conductive fracture measured dips; (f) resistive fracture intensity indicated by the number of fracture planes within 10 m; g) resistive fracture measured dips; (h) sonic velocity and gamma ray logs.

of faults also correlates with the increased clay intensity between ~2,350 and ~2,410 mbsf. Furthermore, a change in orientation of the faults/fractures populations across deduced or observed faults is displayed in the stereonet projections of Figures 5e and 5g and 6e and 6g.

Figures 5h and 6h show gamma ray logging data with only subtle changes, but a general increasing trend with depth that can be explained by the increase in the concentration of radioactive elements in the rock following rock compaction and loss/migration of fluids and rock volume. On the figures major changes in sonic velocity occur along the fault zones both at Hole C0002F and Hole C0002P (Strasser et al., 2013; Tobin et al., 2015). These changes in velocity are not only related to compaction of sediments, but in this tectonic setting have been related to deformation processes (Boston et al., 2016).

4. Discussion

4.1. Localized Fractures and Faults in the Inner Wedge of the Accretionary Prism

The interpretation of logging data from Site C0002, together with the microscopic observations of a number of rock cuttings indicate the existence of localized fractures and faults crosscutting the steep bedding >60° within the accretionary prism. These observations are confirmed by indurated and, in some specific areas, highly fractured mudstones, siltstones, and sandstones observed in some cuttings and spot-cores of Hole C0002P at 2,163.0–2,217.5 mbsf (Tobin et al., 2015). In fact, a single brittle shear zone at around 2,205 mbsf was investigated in detail in the spot-core by Crespo-Blanc (2017). This shear zone is approximately 90 cm long (apparent thickness) and consists of silty claystone and sandstone. Anastomosing cataclastic foliation and the occurrence of various generations of calcite veins that are restricted to the most damaged interval of the cored fault suggest a reiterative history of brecciation and enhanced fluid-rock interaction in the rock. These observations are indicative for several cycles of deformation that most likely took place before the overlying Kumano Basin filling, as the basin sediments are only slightly deformed and tilted (Moore et al., 2015).

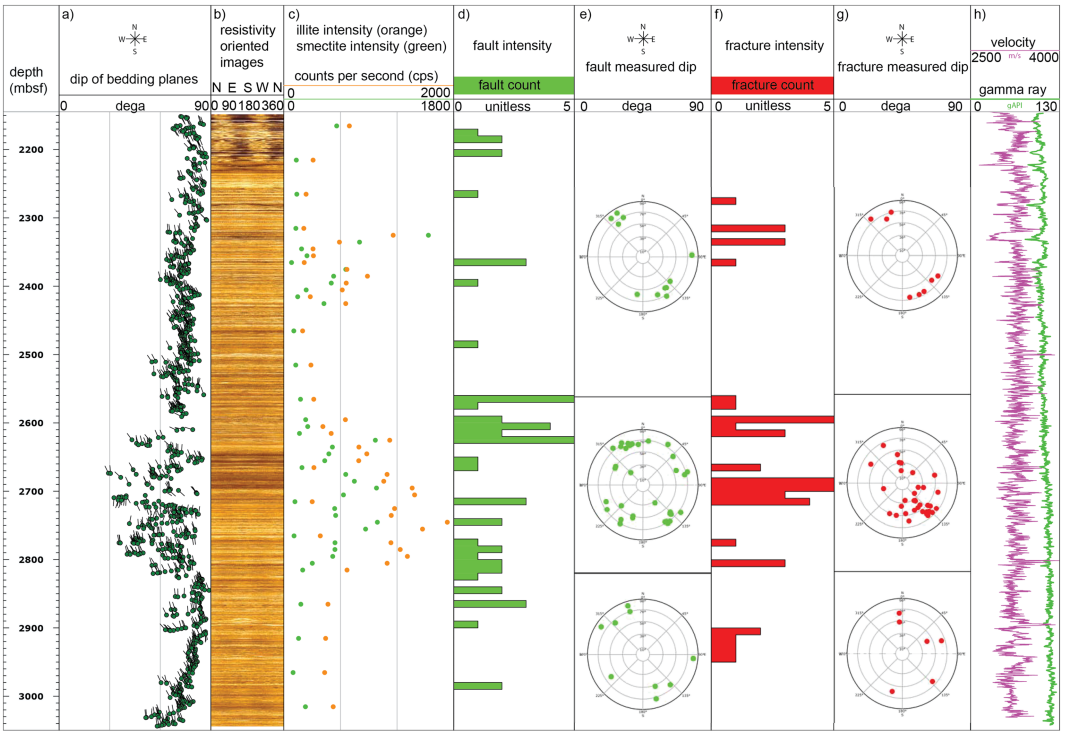

Figure 6. Logging data and mineralogical analyses of Hole C0002P between 2,162.5 and 3,058 mbsf. (a) bedding orientation tadpole plot of bedding planes measured on logging while drilling image; (b) logging while drilling resistivity oriented images; (c) illite and smectite intensity; (d) fault intensity indicated by the number of planes within 10 m; (e) fault measured dips; (f) fracture intensity indicated by the number of fracture planes within 10 m; (g) fracture measured dips; h) sonic velocity and gamma ray logs.

The steep bedding and the high amount of fractures and faults in the accretionary prism was also detected during earlier NanTroSEIZE Expeditions (e.g., Expedition 315 Scientists, 2009 and Expedition 319 Scientists, 2010), but it is clearly recognizable that Hole C0002P shows rather localized areas of fractures and faults between ~2,580 and 2,810 mbsf and between ~2,350 and 2,410 mbsf, whereas fractures in Hole C0002F are more broadly distributed throughout the borehole. The localized abundance of fractures in Hole C0002P concur well with an increase of illite and smectite clay minerals based on the increase of intensity, and shows a clear link between faulting and mineral precipitation. In Hole C0002F, however, the connection between fractures and clay mineral intensity changes is not so obvious, probably because of the mixing effects of cuttings due to the underreamer, which could also have caused additional fractionation in the borehole. Still, some areas with higher amounts of fractures could be determined between ~1,000 and ~1,350 mbsf (conductive fractures), 1,420 mbsf (resistive fractures), and 1,800–2,000 mbsf (conductive fractures).

4.2. Clay Mineral Occurrence and Clay Formation in Fractures and Faults

The main argillaceous products in the hemipelagic mudrock cuttings are clay minerals of detrital origin. Underwood and Song (2016a, 2016b) and Underwood (2017a, 2017b) showed in detail that detrital smectite (approximately 10–50 wt%) and illite (approximately 20–50 wt%) clay minerals are the main phases in the clay size fraction with kaolinite, chlorite and quartz as additional components. They furthermore detected that throughout Hole C0002F, the values of the illite crystallinity index are consistent with diagenesis and anchizone metamorphism, whereas the values in Hole C0002P show that the crystallinity index shifts at about 2,600 mbsf from epizone-anchizone metamorphic conditions to anchizone source conditions. These changing processes at depth can result in various temperature-dependent reactions, such as smectite-illite transition, albitization, hydrocarbon generation, quartz and/or carbonate cementation, development of pressure solution cleavage, and initiation of sediment lithification at low grade temperatures (Moore et al., 2007). In fact, the release of bound water in smectite minerals into the low-permeability mudstone rocks in the

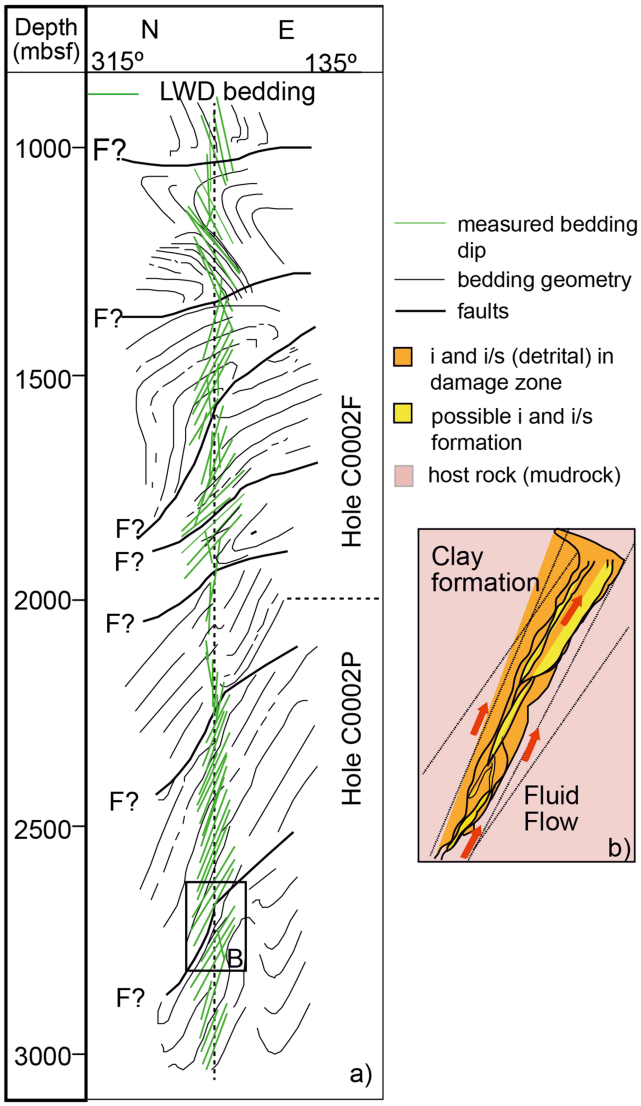

Figure 7. (a) Logging while drilling interpretation NNW-SSE structural sketch showing the orientation of possible faults and fractures in Hole C0002F and C0002P (F?: possible fault zones; green lines: dip of the measured bedding plane; black lines: possible geometry for the measured bedding planes); (b) scenario of possible fluid flow, precipitation of authigenically grown clay minerals and the possible development of clay smear within the fault, which can lead to fault creep activity.

accretionary prism can enhance faulting processes or change the stability of existing faults and fractures due to raising fluid pressure and increasing mineral precipitation. A reason why changes in the amount of clay minerals was not observed in Underwood and Song (2016a, 2016b) and Underwood (2017a, 2017b) could be that the amount of newly formed clay minerals may be too subtle to be detected in the bulk clay size fractions. In our study, we focused on the investigation of solely silty claystone after sorting out the drilling induced aggregates (especially in Hole C0002P).

On the other hand, newly formed clay minerals were observed in Hüpers et al. (2019). Based on detailed clay polytype XRD and TEM analyses, illitic and smectitic mineral phases of both detrital and authigenic origin were detected. This observation is in agreement with our data analysis of the clay size fraction with increasing intensities of illite and smectite rich illite/smectite clay minerals in specific depths intervals. Most importantly, our changes coincide with areas of stronger deformation and higher amounts of faults and fractures. The observations lead to the assumption of enhanced alteration processes, which include the formation of illite and/or illite/smectite minerals (Evans & Chester, 1995). In fact, brittle deformation and clay precipitation are often linked with the circulation of crustal fluids in sedimentary rocks (Faulkner et al., 2010), and has been suggested as a possible explanation for a weak fault behavior (Sibson, 1994; Vrolijk & van der Pluijm, 1999). It is also proposed that dissolution-precipitation reactions may assist the slip along microscopic smectitic phases (Moore & Lockner, 2009; Warr et al., 2014). Finally, a sufficient network of surface coatings of clay minerals may establish the concentration and interconnection of deformation, clay formation and fluid flow (Schleicher et al., 2010).

4.3. Implications for Fluid-Rock Interaction Processes, Fluid Flow, and Fault Behavior

The sediments in the Nankai Trough accretionary prism predominantly deform due to subduction, abrasion and sediment consolidation, whereby fluid pressure rises and fluids are expelled due to fluid-rock interaction processes (Kitajima & Saffer, 2014). These fluids are able to affect the dynamic processes in the accretionary wedge while they become trapped at depth (Kastner et al., 1991; Saffer & Bekins, 1998). The deep sediments of the Nankai Trough that are rich in illite and smectite-rich illite/smectite mixed layers have experienced a fluid release due to consolidation, compaction and diagenesis with accompanied dissolution/precipitation reactions. This is most likely the situation in Hole C0002P between 2,162.5–3,058.4 mbsf, because the settings here change from diagenetic into anchizone source conditions (e.g., Hüpers et al., 2019; Saffer et al., 2008; Underwood, 2017a, 2017b). In fact, the minerals in the cuttings investigated in this study, as well as minerals investigated in core samples by others (e.g., Crespo-Blanc et al., 2017) show distinct alteration features due to dissolution-precipitation reactions (Figures 3 and 4), and both quartz and feldspar clasts have highly sutured grain boundaries that are attributed to intense dissolution. Clay formation occurs particularly in the areas of strong fracturing and faulting (2,350 mbsf, 2,600 and 2,800 mbsf in Hole C0002P). Here, the fluid pathways are notably controlled by the occurrence and the orientation of the deeply dipping faults and fractures, as with increasing sediment overburden and degree of particle orientation accompanied by loss of porosity and permeability, and the fluid flow can easily be channeled and focused.

Both smectitic and illitic clay minerals, which are undoubtable abundant in the accretionary prism, have been used to explain the low long-term strength and mechanical behavior of the Nankai Trough accretionary prism. Especially the water-rich mineral assemblages smectite located along the main fault are prime

candidates to explain the mechanical weakness of the structure (e.g., Brown et al., 2003; Moore & Saffer, 2001). In this context, we envisage two different mechanisms of clay formation and implication for fault-weakening in the fault zones of the accretionary prism, (i) reworking of the material (e.g., Holland et al., 2006) and (ii) clay smear along fractures (e.g., Vrolijk et al. (2016)). Based on our observations, both deformation features such as fractures and faults occur in the rock grains, as well as dissolution/precipitation features. On the other hand, a cataclastic breakdown by repeated grain fracturing in these samples is only minor, and intense dissolution and precipitation reactions is dominant in the drilled part of the accretionary prism. These observations favor the occurrence of clay smear due to precipitation of authigenic clay minerals. Based on the orientation and location of faults and fractures in the drillholes investigated in the Nankai Trough, Figure 7 describes a possible scenario of fluid flow, precipitation of authigenically grown clay minerals and the development of clay gouge within the fault, which can lead to fault creep activity.

Similar to the scenario of clay in fractures and faults in the Nankai Trough accretionary prism, the importance of smectitic clay and clay coatings has been reported in the Barbados accretionary prisms and in transform faults such as the San Andreas Fault (Lockner et al., 2011; Schleicher et al., 2010; Wu et al., 1975). In the latter, the precipitation of saponite clay minerals makes the fault particularly weak. Such mineral dissolution and neomineralization processes of smectite phases along active faults and fractures is a process that probably continues during creep and fault activity, until a seismic event abandons the weak strand and produces new fracture surfaces in a nearby area. This distinct link between localized abundant faults and fractures accompanied by the precipitation of clay minerals shows that clay minerals play a key role in influencing the mechanical behavior and creep in shallow fault zones. However, at some point in the diagenetic and metamorphic history of the subducted sediments, smectite will completely transform into illite as part of the ongoing consolidation process, and the sedimentary package will strengthen. In fact, diagenetic conditions that include smectite transition into illite has already started in Hole C0002P (Underwood, 2017a). This suggests that the onset of seismicity may be related to a strengthening of material during prograde metamorphism of smectite.

5. Conclusions

Based on our combined mineralogical and microscopic analyses, together with the interpretation of LWD oriented images ansd geophysical log data, we detected a connection between the abundance of illite and smectite clay minerals and the occurrence of localized fractures and faults in the part of the accretionary prism drilled during Expedition 338 and 348. LWD image interpretation results indicate strong tectonic deformation of the accretionary prism sediments, characterized by steep bedding and a large number of fractures and faults. Both drill holes show distinct areas of intense fracturing and faulting within a very clay-dominated lithology. Illite and smectite rich illite/smectite are the most common clay minerals. The presence of faults as a differential feature in Hole C0002P suggests these would be the most recent and probably active structures within this section of the accretionary prism and would confirm a relationship with clay mineral analyses results.

Acknowledgments
We would like to thank Sean Toczko, Lena Maeda, Yusuke Kubo, Nobu Eguchi, the Expedition Scientists, and the whole crew onboard *D/V Chikyu* for their excellent support during IODP Expeditions 338 and 348. ECORD, USAC, and IODP are greatly acknowledged for participation of the Expeditions. Very helpful comments and the review of Hiroko Kitajima and an anonymous reviewer significantly improved this manuscript. Thank you to Ben van der Pluijm and the Electron Microbeam Analysis Laboratory (EMAL), Central Campus, University of Michigan for using their equipment. M. J. Jurado research was supported by grant CGL2010-21568 from the Spanish Ministry of Science and Innovation. Raw data are stored in the "GFZ Data Services" (Schleicher & Jurado, 2019).

References

Baba, T., Cummins, P. R., Hori, T., & Kaneda, Y. (2006). High precision slip distribution of the 1944 Tonankai earthquake inferred from tsunami waveforms: Possible slip on a splay fault. *Tectonophysics*, *426*(2-3), 119–134. https://doi.org/10.1016/j.tecto.2006.02.015

Bird, P. (1984). Hydration-phase diagrams and friction of montmorillonite under laboratory and geologic conditions, with implications for shale compaction, slope stability, and strength of fault gouge. *Tectonophysics*, *107*(3-4), 235–260. https://doi.org/10.1016/0040-1951(84)90253-1

Boston, B., Moore, G. F., Jurado, M. J., & Sone, H. (2016). Deformation of the Nankai Trough inner accretionary prism: The role of inherited structures. *Geochemistry, Geophysics, Geosystems*, *17*, 485–500. https://doi.org/10.1002/2015GC006185

Brown, K. M., Kopf, A., Underwood, M. B., & Weinberger, J. L. (2003). Compositional and fluid pressure controls on the state of stress on the Nankai subduction thrust: A weak plate boundary. *Earth and Planetary Science Letters*, *214*, 589–603. https://doi.org/10.1016/S0012-821X(03)00388-1

Caine, J. S., Evans, J. P., & Forster, C. B. (1996). Fault zone architecture and permeability structure. *Geology*, *24*(11), 1025–1028. https://doi.org/10.1130/0091-7613(1996)024<1025:FZAAPS>2.3.CO;2

Crespo-Blanc, A. (2017). Data report: A brittle (normal?) shear zone from Hole C0002P: Deformation structures and their relationship with calcite veins (IODP Expedition 348, Nankai Trough accretionary prism). In H. Tobin, T. Hirose, D. Saffer, S. Toczko, L. Maeda, Y. Kubo, & the Expedition 348 Scientists (Eds.), *Proceedings of the Integrated Ocean Drilling Program* (Vol. 348, pp. 1–25). College Station, TX: Integrated Ocean Drilling Program. https://doi.org/10.2204/iodp.proc.348.205.2017

Davis, D., Suppe, J., & Dahlen, F. A. (1983). Mechanics of fold-and-thrust belts and accretionary wedges. *Journal of Geophysical Research*, *88*(B2), 1153–1172. https://doi.org/10.1029/JB088iB02p01153

Evans, J. P., & Chester, F. M. (1995). Fluid-rock interaction in faults of the San Andreas system: Inferences from San Gabriel fault rock geochemistry and microstructures. *Journal of Geophysical Research*, *100*(B7), 13,007–13,030. https://doi.org/10.1029/94JB02625

Faulkner, D. R., Jackson, C. A. L., Lunn, R. J., Schlische, R. W., Shipton, Z. K., Wibberley, C. A. J., & Whithjack, M. O. (2010). A review of recent developments concerning the structure, mechanics and fluid flow properties of fault zones. *Journal of Structural Geology*, *32*(11), 1557–1575. https://doi.org/10.1016/j.jsg.2010.06.009

Holland, M., Urai, J. L., van der Zee, W., Stanjek, H., & Konstanty, J. (2006). Fault gouge evolution in highly overconsolidated claystone. *Journal of Structural Geology*, *28*(2), 323–332. https://doi.org/10.1016/j.jsg.2005.10.005

Hüpers, A., Grathoff, G., Warr, L. N., Wemmer, K., Spinelli, G., & Underwood, M. B. (2019). Spatiotemporal characterization of smectite-to-illite diagenesis in the Nankai Trough accretionary prism reveladed by samples from 3 km below seafloor. *Geochemistry, Geophysics, Geosystems*, *20*, 933–951. https://doi.org/10.1029/2018GC008015

Kanamori, H. (1972). Tectonic implications of the 1944 Tonankai and the 1946 Nankaido earthquakes. *Physics of the Earth and Planetary Interiors*, *5*, 129–139. https://doi.org/10.1016/0031-9201(72)90082-9

Kastner, M., Elderfield, H., & Martin, J. B. (1991). Fluids in convergent margins: What do we know about their composition, origin, role in diagenesis and importance for oceanic chemical fluxes? *Philosophical Transactions of the Royal Society of London*, *335*(1638), 243–259.

Kimura, G., Kitamura, Y., Hashimoto, Y., Yamaguchi, A., Shibata, T., Ujiie, K., & Okamoto, S. (2007). Transition of accretionary wedge structures around the up-dip limit of the seismogenic subduction zone. *Earth and Planetary Science Letters*, *255*(3-4), 471–484. https://doi.org/10.1016/j.epsl.2007.01.005

Kinoshita, M., Tobin, H., Ashi, J., Kimura, G., Lallemant, S., Screaton, E. J., et al. (2009). *Proc. IODP, 314/315/316*. Washington, DC: Integrated Ocean Drilling Program Management International, Inc. https://doi.org/10.2204/iodp.proc.314315316.114.2009

Kitajima, H., & Saffer, D. M. (2014). Consolidation state of incoming sediments to the Nankai Trough subduction zone: Implications for sediment deformation and properties. *Geochemistry, Geophysics, Geosystems*, *15*, 2821–2839. https://doi.org/10.1002/2014GC005360

Lockner, D. A., Morrow, C., Moore, D., & Hickman, S. (2011). Low strength of deep San Andreas fault gouge from SAFOD core. *Nature*, *472*(7341), 82–85. https://doi.org/10.1038/nature09927

Moore, D., & Lockner, D. A. (2009). Friction of the smectite clay montmorillonite: A review and interpretation of data. In T. H. Dixon, & C. Moore (Eds.), *the seismogenic zone of subduction thrust faults*, *Margins Theor. Exp. Earth Sci. Ser., 2*, (Vol. 11, pp. 317–345). New York: Columbio University Press.

Moore, D. M., & Reynolds, R. C. (1997). *X-ray diffraction and the identification and analysis of clay minerals*, (p. 378). Oxford: Oxford University Press.

Moore, G. F., Boston, B. B., Strasser, M., Underwood, M. B., & Ratliff, R. A. (2015). Evolution of tectono-sedimentary systems in the Kumano Basin, Nankai Trough forearc. *Marine and Petroleum Geology*, *67*, 604–616. https://doi.org/10.1016/j.marpetgeo.2015.05.032

Moore, G. F., Kanagawa, K., Strasser, M., Dugan, B., Maeda, L., Toczko, S., & the IODP Expedition 338 Scientific Party (2014). IODP Expedition 338: NanTroSEIZE Stage 3: NanTroSEIZE plate boundary deep riser 2. *Scientific Drilling*, *17*, 1–12. https://doi.org/10.5194/sd-17-1-2014

Moore, J. C., Rowe, C., & Meneghini, F. (2007). How accretionary prisms elucidate seismogenesis in subduction zones. In T. H. Dixon & J. C. Moore (Eds.). The Seismogenic Zone of Subduction Thrust Faults (p. 288–315). New York: Columbia University Press. https://doi.org/10.7312/dixo13866-010

Moore, J. C., & Saffer, D. (2001). Updip limit of the seismogenic zone beneath the accretionary prism of southwest Japan: An effect of diagenetic to low-grade metamorphic processes and increasing effective stress. *Geology*, *29*(2), 183–186. https://doi.org/10.1130/0091-7613(2001)029<0183:ULOTSZ>2.0.CO;2

Moore, J. C., & Vrolijk, P. (1992). Fluids in accretionary prisms. *Reviews of Geophysics*, *30*(2), 113–135. https://doi.org/10.1029/92RG00201

Park, J.-O., Tsuru, T., Kodaira, S., Cummins, P. R., & Kaneda, Y. (2002). Splay fault branching along the Nankai subduction zone. *Science*, *297*, 1157–1160. https://doi.org/10.1126/science.1074111

Raimbourg, H., Vacelet, M., Ramboz, C., Famin, V., Augier, R., Palazzin, G., et al. (2015). Fluid circulation in the depths of accretionary prisms: An example of the Shimanto Belt, Kyushu, Japan. *Tectonophysics*, *655*, 161–176. https://doi.org/10.1016/j.tecto.2015.05.023

Ryan, W. B., Carbotte, S. M., Coplan, J. O., O'Hara, S., Melkonian, A., Arko, R., & Zemsky, R. (2009). Global multi-resolution topography synthesis. *Geochemistry, Geophysics, Geosystems*, *10*, Q03014. https://doi.org/10.1029/2008GC002332

Saffer, D. M., & Bekins, B. A. (1998). Episodic fluid flow in the Nankai accretionary complex: Timescale, geochemistry, flow rates and fluid budget. *Journal of Geophysical Research*, *103*(B12), 30,351–30,370. https://doi.org/10.1029/98JB01983

Saffer, D. M., Underwood, M. B., & McKiernan, A. W. (2008). Evaluation of factors controlling smectite transformation and fluid production in subduction zones: Application to the Nankai Trough. *Island Arc*, *17*(2), 208–230. https://doi.org/10.1111/j.1440-1738.2008.00614.x

Schleicher, A. M., & Jurado, M. (2019). XRD analyses on cuttings samples from IODP Expeditions 338 and 348 (Nankai Trough accretionary prism)., GFZ Data Services : Potsdam

Schleicher, A. M., van der Pluijm, B. A., & Warr, L. N. (2010). Nano-coatings of clay and creep of the San Andreas fault at Parkfield, California. *Geology*, *38*(7), 667–670. https://doi.org/10.1130/G31091.1

Seno, T., Stein, S., & Gripp, A. E. (1993). A model for the motion of the Philippine Sea plate consistent with Nuvel-1 and geological data. *Journal of Geophysical Research*, *98*(B10), 17,941–17,948. https://doi.org/10.1029/93JB00782

Sibson, R. H. (1994). Crustal stress, faulting and fluid flow. In J. Parnell (Ed.), *Geofluids: Origin, Migration and Evolution of fluids in sedimentary basins*, *Geological Society Special Publication* (Vol. 78, pp. 69–84). London.

Strasser, M., Dugan, B., Kanagawa, K., Moore, G. F., Toczko, S., Maeda, L., et al. (2013). Proceedings of the Integrated Ocean Drilling Program (Vol. 338), Yokohama (Integrated Ocean Drilling Program). https://doi.org/10.2204/iodp.proc.338.2014

Strasser, M., Moore, G. F., Kimura, G., Kitamura, Y., Kopf, A. J., Lallemant, S., et al. (2009). Origin and evolution of a splay fault in the Nankai accretionary wedge. *Nature Geoscience*, *2*(9), 648–652. https://doi.org/10.1038/ngeo609

Tobin H., Hirose T., Saffer D., Toczko S., Maeda L., Kubo Y., & the Expedition 348 Scientists (2015). Proceedings of the Integrated Ocean Drilling Program (Vol. 348), College Station, TX: Integrated Ocean Drilling Program. https://doi.org/10.2204/iodp.proc.348.2015

Tobin, H., & Kinoshita, M. (2006). NanTroSEIZE: The IODP Nankai Trough Seismogenic Zone Experiment. *Scientific Drilling*, *2*, 23–27. https://doi.org/10.2204/iodp.sd.2.06.2006

Toki, T., Higa, R., Ijiri, A., Tsunogai, U., & Ashi, J. (2014). Origin and transport of pore fluids in the Nankai accretionary prism inferred from chemical and isotopic compositions of pore water at cold seep sites off Kumano. *Earth, Planets and Space*, *66*(1), 137. https://doi.org/10.1186/s40623-014-0137-3

Underwood, M. (2017a). Data report: Clay mineral assemblages and illite/smectite diagenesis in cuttings from Hole C0002P, IODP Expedition 238, Nankai Trough accretionary prism. In H. Tobin, T. Hirose, D. Saffer, S. Toczko, L. Maeda, Y. Kubo, & the Expedition 348 Scientists (Eds.), *Proceedings of the Integrated Ocean Drilling Program* (Vol. 348, pp. 1–17). College Station, TX: Integrated Ocean Drilling Program.

Underwood, M. (2017b). Data report: Clay mineral assemblages in cuttings from Hole C0002N, IODP Expedition 348, Nankai Trough accretionary prism. In H. Tobin, T. Hirose, D. Saffer, S. Toczko, L. Maeda, Y. Kubo, & the Expedition 348 Scientists (Eds.), *Proceedings of the Integrated Ocean Drilling Program* (Vol. 348, pp. 1–16). College Station, TX: Integrated Ocean Drilling Program.

Underwood, M., & Song, C. (2016a). Data report: Clay mineral assemblages in cores from Hole C0002P, IODP Expedition 348, Nankai Trougeh accretionary prism. Isn. In H. Tobin, T. Hirose, D. Saffer, S. Toczko, L. Maeda, Y. Kubo, & the Expedition 348 Scientists (Eds.), *Proceedings of the Integrated Ocean Drilling Program* (Vol. 348, pp. 1–13). College Station, TX: Integrated Ocean Drilling Program.

Underwood, M., & Song, C. (2016b). Data report: Clay mineral assemblages in cuttings from Hole C0002F, IODP Expedition 338, Nankai Trough accretionary prism. In M. Strasser, B. Dugan, K. Kanagawa, G. F. Moore, S. Toczko, L. Maeda, & the Expedition 338 Scientists (Eds.), (Vol. *338*). College Station, TX: Proceedings of the Integrated Ocean Drilling Program.

Underwood, M. B. (2007). Sediment inputs to subduction zones. In T. H. Dixon, & J. C. Moore (Eds.), *The seismogenic zone of subduction thrust faults*, (pp. 42–85). New York: Columbia University Press.

Underwood, M. B., & Pickering, K. T. (1996). Clay-mineral provenance, sediment dispersal patterns, and mudrock diagenesis in the Nankai accretionary prism, Southwest Japan. *Clays and Clay Minerals*, *44*(3), 339–356. https://doi.org/10.1346/CCMN.1996.0440304

Vrolijk, P. (1990). On the mechanical role of smectite in subduction zones. *Geology*, *18*(8), 703–707. https://doi.org/10.1130/0091-7613(1990)018<0703:OTMROS>2.3.CO;2

Vrolijk, P., & van der Pluijm, B. A. (1999). Fault gouge. *Journal of Structural Geology*, *21*, 1039–1048. https://doi.org/10.1015/S0191-8141(99)00103-0s

Vrolijk, P. J., Urai, J. L., & Kettermann, M. (2016). Clay smear: Review of mechanisms and applications. *Journal of Structural Geology*, *86*, 95–152. https://doi.org/10.1016/j.jsg.2015.09.006

Warr, L. N., Wojatschke, J., Carpenter, B. M., Marone, C., Schleicher, A. M., & van der Pluijm, B. A. (2014). A "slice-and view" (FIB-SEM) study of clay gouge from the SAFOD creeping section of the San Andreas Fault at approximately 2.7 km depth. *Journal of Structural Geology*, *69*, 234–244. https://doi.org/10.1016/j.jsg.2014.10.006

Wirth, R. (2009). Focused Ion Beam (FIB) combined with SEM and TEM: Advanced analytical tools for studies of chemical composition, microstructure and crystal structure in geomaterials on a nanometre scale. *Chemical Geology*, *261*(3–4), 217–229. https://doi.org/10.1016/j.chemgeo.2008.05.019

Wu, F. T., Blatter, L., & Robertson, H. (1975). Clay gouges in the San Andreas fault system and their possible implications. *Pure and Applied Geophysics*, *133*, 87–95.